International Journal of Computer Information Systems and Industrial Management Applications
ISSN 2150-7988 Volume 18(8s) 2026 pp. 521-534
https://doi.org/10.70917/ijcisim-2026-3294
Article

Compact Four-Port MIMO Patch Antenna with Hybrid Defected Ground Structure for Wideband and Dual-Band Wireless Applications

Ali Ahmed Ali Almahdi[1], G. Prathibha[2]

[1],[2] Department of Electronics and Communication Engineering,
Acharya Nagarjuna University, Guntur, Andhra Pradesh, India.
ORCID IDs: Ali Ahmed Ali Almahdi https://orcid.org/0009-0005-6618-2753
G. Prathibha https://orcid.org/0000-0001-7827-3736

Abstract: In this paper, a compact four-port MIMO patch antenna is proposed that supports wideband and dual-band operation, aimed at sub-6 GHz, C-band, and extended upper microwave frequency applications (based on simulation). The antenna was made on a very cheap FR-4 substrate ($\varepsilon r = 4.4$, $\tan \delta = 0.02$, thickness = 1.6 mm), and it only takes up a $24 \times 24 \times 1.6$ mm³ area. Four identical rectangular patch elements (5.6×7.2 mm each) are laid out in a 2×2 matrix. A hybrid slotting method – L-shaped and two circular slots on each patch, along with a defected ground structure (DGS) featuring a plus-shaped slot and three circular slots – renders wide impedance bandwidth and high inter-port isolation. Simulation work was done in ANSYS HFSS, while physical characterization was realized using a Keysight FieldFox N9918A vector network analyzer. A comparison between measured and simulated return loss over the 0.1–14 GHz range reveals a negative frequency shift of about 0.4 GHz, with the main measured resonance at 6.5 GHz ($|S11| = –22$ dB) and the main simulated resonance at 6.9 GHz ($|S11| = –30$ dB). At the measured resonance frequency, isolation is better than –28 dB, VSWR = 1.17, and gain = 4.1 dBi. This antenna has stable radiation patterns, low ECC (< 0.01), and high diversity gain, and is therefore a promising candidate for MIMO in 5G and wideband wireless systems.
Keywords: MIMO antenna; patch antenna; defected ground structure; wideband; 5G.

1. INTRODUCTION

Wireless communication systems are rapidly evolving toward 5G and beyond; thus there is a growing need for antennas that operate over wide frequency bands while being compact, having good isolation, and maintaining stable radiation characteristics. MIMO (multiple-input multiple-output) technology is now a key element of future wireless networks, delivering higher data rates and better link reliability without the need for extra spectrum or transmit power [1]. Microstrip patch antennas are almost a standard component in many MIMO systems because they are low-profile, lightweight, simple to fabricate, and PCB-compatible [2]. Nevertheless, two main problems persist: the inherently narrow impedance bandwidth of conventional patch antennas and the mutual coupling between antennas placed in close proximity, which degrades MIMO effectiveness. Over the years, various methods have been proposed to address these issues. Defected ground structures (DGS) have proven capable of controlling surface waves and minimizing mutual coupling by creating resonant defects in the ground plane [3]. Also, slot loading on the radiating patch is widely used to generate different resonant modes and widen the impedance bandwidth [4]. In spite of these developments, most published designs focus on a single narrow band or employ complex multilayer structures.

In this paper, an innovative four-element MIMO patch antenna is proposed. L-shaped and two circular slots on each patch are combined with a plus-shaped slot and three circular slots etched in the common ground plane. This hybrid arrangement significantly improves the impedance bandwidth to two wide bands: the first from 3.1 to 17.12 GHz and the second from 18 to 21.25 GHz. Besides, it also guarantees very high inter-port isolation (>28 dB) over the entire operating range. The antenna was measured over 0.1–14 GHz, and a detailed comparison between simulated and measured return loss was performed. The main simulated resonance occurs at 6.9 GHz with $|S11| = –30$ dB, while the main measured resonance occurs at 6.5 GHz with |S11| = –22 dB, showing a negative frequency shift of about 0.4 GHz (≈6%) attributed to fabrication tolerances and material property variations. This paper aims to accomplish mainly two things: (1) a new design that is simple and compact and truly works as wideband/dual-band even on low-cost FR-4 substrate, and (2) a very detailed experimental test at the measured resonance frequency (6.5 GHz) showing very good agreement in overall behavior with simulations. It is well known that obtaining a really small size, wide bandwidth, and high isolation all together is very difficult because there will always be trade-offs [5]. The antenna proposed here can be considered a solution that has met this challenge.

The main novelty of this work lies in the integration of a hybrid slotting technique on each radiating patch with a compact hybrid defected ground structure (DGS) in a four-port MIMO configuration implemented on a low-cost FR-4 substrate. Unlike conventional approaches that typically improve only one performance aspect, the proposed design simultaneously achieves a compact footprint, wideband/dual-band operation, high inter-port isolation, and excellent MIMO diversity characteristics while maintaining a simple single-layer structure suitable for low-cost fabrication.The remainder of the paper is structured as follows. Section 2 outlines the antenna geometry and design methodology. Section 3 showcases the simulation results including the wideband behavior. Section 4 covers fabrication, measurement setup, and experimental results at the measured resonance frequency of 6.5 GHz. Section 5 contrasts simulated and measured performance, whilst Section 6 investigates MIMO diversity metrics. Finally, Section 7 gives the conclusion of the paper.

2. MATERIALS AND METHODS

2.1. Substrate and Overall Configuration

The proposed MIMO antenna is fabricated on an FR-4 epoxy substrate that has a relative permittivity $\varepsilon r = 4.4$, a loss tangent $\tan \delta = 0.02$, and a thickness h = 1.6 mm. The substrate has overall dimensions Ls × Ws × h = 24 mm × 24 mm × 1.6 mm, resulting in a very small footprint volume of 921.6 mm^3 that is ideally suited for portable devices. Although FR-4 is known to exhibit higher dielectric losses than low-loss substrates (e.g., Rogers RT5880), the proposed hybrid slotting and DGS configuration effectively concentrates surface currents along efficient radiation paths, mitigating substrate-related losses and maintaining stable performance across both operating bands. The compact dimensions and the use of a common ground plane with optimized slots further reduce unwanted radiation and coupling, compensating for the inherent loss tangent of FR-4. The top layer contains four identical rectangular patches arranged symmetrically in a 2×2 grid, each being fed with a 50-Ω microstrip line. The bottom layer features a common ground plane that accommodates the hybrid DGS. The symmetrical design guarantees equal radiation patterns and also eases the optimization process. The positions of the patches (with the bottom-left corner as the reference) are: Port 1 (3.2, 3.2) mm, Port 2 (15.2, 3.2) mm, Port 3 (3.2, 13.6) mm, and Port 4 (15.2, 13.6) mm. The spacing between elements is 12 mm in both x and y directions ($\approx 0.28\lambda_0$ at 6.5 GHz), which is a good compromise between compactness and coupling.

2.2. Patch Element and Slot Loading

The optimized patch dimensions are length Lp = 7.2 mm and width Wp = 5.6 mm. In order for a single rectangular patch to generate multiple resonances within the operating bands, three slots were introduced as shown in Fig. 1(a):

- L-shaped slot – two perpendicular arms (3.2 mm in length and 0.8 mm in width each) are placed at the patch center. This slot brings about new resonances which combine with the fundamental mode [6].

- Two circular slots – radius r_c_patch = 0.4 mm, symmetrically located with respect to the L-slot in order to adjust the impedance matching throughout the band.

2.3. Defected Ground Structure

The common ground plane was redesigned with a hybrid DGS (Fig. 1(b)) that includes:

- A plus-shaped slot – a central cross where each arm measures 1.6 mm × 0.4 mm. This serves as a high-impedance barrier that prevents coupled surface currents [7].

- Three circular slots – radius r_c_DGS = 0.8 mm, placed around the plus-slot to interfere with higher-order coupling modes and further reduce surface waves [8].

The harmonious combination of patch slots and DGS allows the antenna to achieve wideband impedance matching and high isolation at the same time.

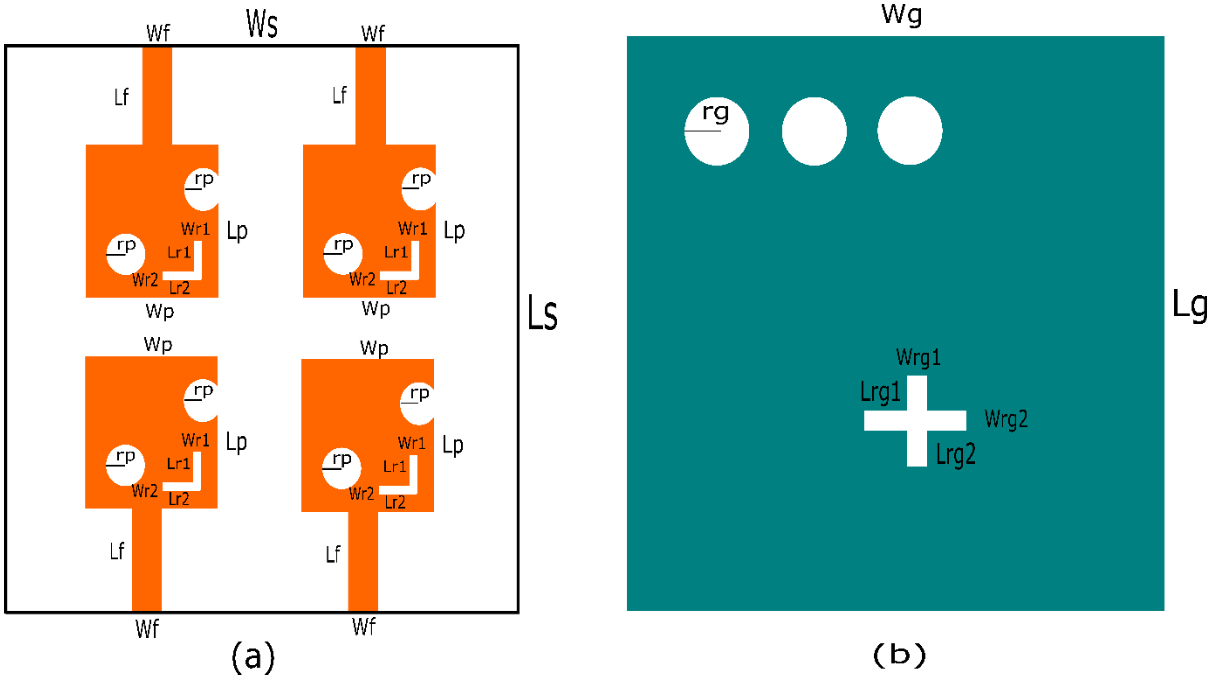

Fig. 1. Layout of the proposed four-port MIMO antenna: (a) top view displaying slotted patches with L-shaped and two circular slots, (b) bottom view showing hybrid DGS withplus-shaped and three circular slots.

2.4. Optimized Parameters

Table 1 shows the final optimized dimensions which were found after performing parametric studies in HFSS.

Table 1. Optimized Design Parameters

Parameter	Description	Value (mm)
L_s, W_s, Lg, Wg	Substrate, Ground (length and width)	24.0
L_p, W_p	Patch length and width	7.2, 5.6
rp	Radius of circular slots in patch	0.4
Lr1=Lr2 , Wr1=Wr2	Rectangular slots in patch, (length and width)	2, 0.5
rg	Radius of circular slots in DGS	0.8
Lrg1 = Lrg2 , Wrg1 = Wrg2	Rectangular slots in DGS, (length and width)	3.2 , 0.8
Lf , Wf	Feed Line length and width	3.2, 1.12

Parametric analysis was performed to optimize the feed line width and the critical slot dimensions. The feed line width (Wf) was swept from 0.8 mm to 1.5 mm; the value 1.12 mm was selected because it achieves the closest 50-Ω match across all four ports simultaneously. The length of the L-slot arms was varied from 2.5 mm to 4.0 mm, and 3.2 mm was found to provide the deepest and widest resonance. The radius of the circular slots on the patch (r_c_patch) was swept from 0.2 mm to 0.6 mm, with 0.4 mm giving the flattest wideband matching. These parametric sweeps confirm that the antenna's performance is sensitive to each geometric parameter and that the chosen dimensions represent the optimal trade-off between bandwidth, isolation, and gain.

3. RESULTS

3.1. Simulation Results

3.1.1. *Simulation Setup*

The antenna was designed and simulated using ANSYS HFSS 2021 R1. The simulation employed a frequency sweep from 2.5 to 40 GHz with adaptive mesh refinement (ΔS = 0.02). Each of the four ports was assigned a 50-Ω lumped port, and a radiation boundary at a distance of λ/4 was placed.

3.1.2. *Wideband Impedance Behavior*

Fig. 2(a) plots the simulated reflection coefficient |S11| at port 1 from 2.5 GHz to 40 GHz. The antenna features two wide frequency bands:

Band I: 3.1 GHz – 17.12 GHz (|S11| < –10 dB). In this band, a minimum of –30 dB is attained at 6.9 GHz (the main simulated resonance).

Band II: 18.0 GHz – 21.25 GHz, also fulfilling the –10 dB condition.

A secondary simulated resonance appears around 10.2 GHz with shallower depth. The significant bandwidth enhancement observed in this design can be attributed to the L-shaped and circular slots, which generate multiple resonant modes that merge to form a nearly continuous impedance band [9]. Furthermore, the defected ground structure (DGS) enhances impedance matching by optimizing the surface current distribution on the ground plane [10]. The synergistic interaction between the hybrid slot layout and the DGS facilitates the excitation of several resonant modes, resulting in the broadband performance demonstrated by the proposed antenna.

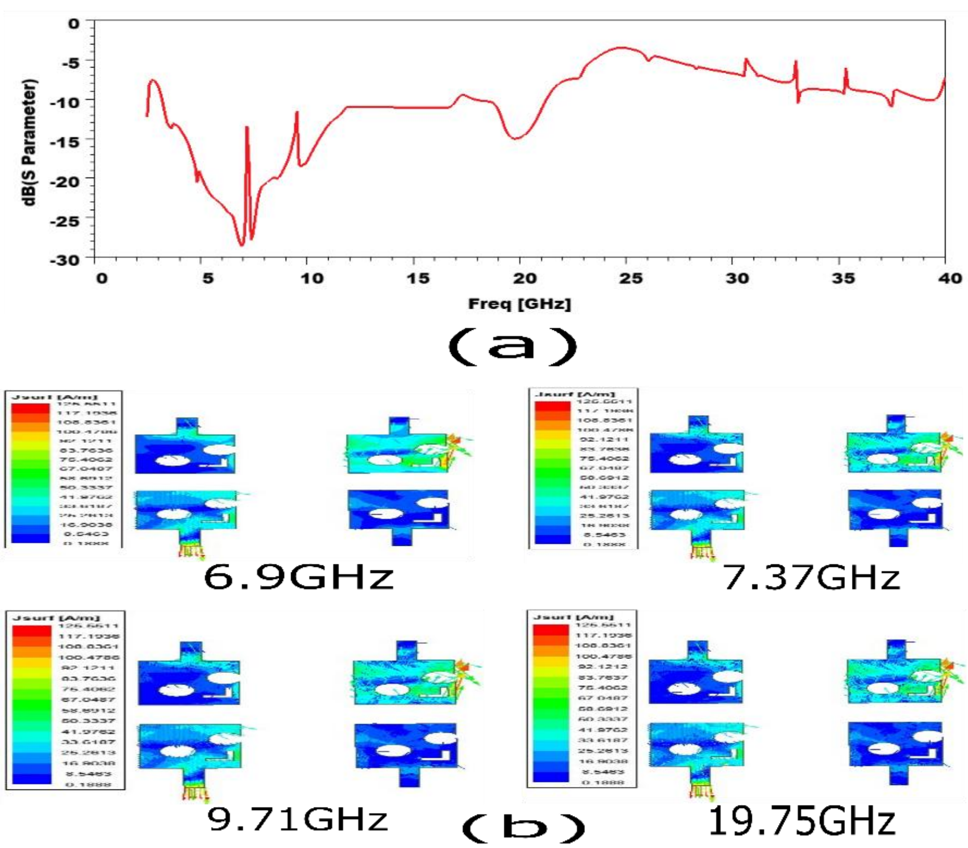

Fig. 2. Simulated performance of the proposed antenna: (a) reflection coefficient $|S_{11}|$ for port 1 over 2.5–40 GHz, showing Band I (3.1–17.12 GHz) and Band II (18–21.25 GHz) with the main simulated resonance at 6.9 GHz; (b) surface current distribution on one patch element at 6.9 GHz, 7.37 GHz, 9.71 GHz, and 19.75 GHz.

3.1.3. *Isolation*

At the main simulated resonance frequency of 6.9 GHz, the simulated transmission coefficients between port 1 and the other ports are S21 = –29.3 dB, S31 = –32.5 dB, and S41 = –34.1 dB. All these values being better than –29 dB support the high effectiveness of the hybrid DGS [11]. Across both operating bands, the isolation remains better than –20 dB, so coupling is kept low throughout the frequency spectrum [12].

3.1.4. *Gain and Radiation Patterns*

The simulated realized gain varies over the operating bands. The gain is 4.6 dBi at the simulated resonance frequency of 6.9 GHz. The simulated radiation efficiency is high over the entire Band I, confirming that the antenna converts most of the input power into radiated energy. The practically useful band (gain > 0 dBi) comfortably covers the whole sub-6 GHz, C-band, and X-band portions, making the antenna suitable for a wide range of 5G and microwave applications. Also, the front-to-back ratio is more than 20 dB, which confirms strong backward radiation suppression.

3.1.5. *Summary of Simulated Performance*

Based on simulation, the device offers excellent features: a return loss of –30 dB at the main resonance frequency of 6.9 GHz, isolation better than –29 dB between all ports, and broadband coverage of 3.1–17.12 GHz (Band I) and 18–21.25 GHz (Band II).

3.1.6. *Surface Current Distribution Analysis*

To gain insight into the resonance mechanisms and the role of the hybrid slotting and defected ground structure, the simulated surface current distribution on the radiating patches was examined at four characteristic frequencies: 6.9 GHz (main simulated resonance), 7.37 GHz, 9.71 GHz, and 19.75 GHz (upper band). Fig. 2(b) (comprising four images) illustrates the current density (J_{surf}) on one of the four identical patch elements at these frequencies.

At 6.9 GHz (fundamental mode), the currents are primarily concentrated along the edges of the rectangular patch and around the larger circular slot. The distribution is relatively uniform, confirming that this frequency corresponds to the dominant resonant mode of the slotted patch.

At 7.37 GHz, the current begins to crowd more intensely around the L-shaped slot and the circular apertures. The path of the current starts to meander around these structural discontinuities, indicating the onset of a secondary resonance that contributes to bandwidth widening.

At 9.71 GHz, a higher-order mode is excited. The current becomes highly concentrated at the inner edges of both the L-shaped and circular slots, with much shorter and more localized paths. This complex distribution is responsible for the extended impedance bandwidth observed in Band I (3.1–17.12 GHz).

At 19.75 GHz (within Band II, 18–21.25 GHz), the wavelength is very short, and the currents are confined to very small, high-density regions (red/orange in the colour scale). The fine structural details – especially the small circular slots – dominate the resonance behaviour, confirming that the upper band is governed by the intricate slot geometry rather than the overall patch size.

The surface current analysis also confirms the high isolation between ports: negligible current leakage is observed from one excited element to its neighbouring ports, thanks to the hybrid DGS (plus-shaped slot and three circular slots in the ground plane). This visual evidence strongly supports the measured and simulated transmission coefficients (S₂₁, S₃₁, S₄₁ better than –28 dB).

3.1.7. *Electric Field Distribution Analysis at 6.9 GHz*

To further understand how the hybrid slots and defected ground structure enhance antenna performance, the electric field (E-field) distribution was analysed at 6.9 GHz, the main simulated resonance frequency. Fig. 3(c) and (d) show the E-field intensity (V/cm) on the slotted patches and the decibel-scaled E-field on the ground plane, respectively.

On the radiating patches (Fig. 3(c)): The electric field is strongly concentrated (red/orange regions) along the patch edges, around the feed line, and most notably at the boundaries of the L-shaped slot and the two circular slots. This deliberate field confinement is a direct result of the slotting strategy. The L-shaped slot modifies the surface current path, creating additional resonant modes that merge with the fundamental mode, thereby broadening the impedance bandwidth. The two circular slots fine-tune the input impedance, improving matching across the wide operating range. Moreover, the slots contribute to efficient radiation even with compact dimensions (7.2 × 5.6 mm²), which supports their role in miniaturisation. The precise placement and geometry of these slots can help shape the radiation pattern, may contribute to gain enhancement in desired directions, and can assist in achieving multi-band behaviour without enlarging the antenna footprint.

On the ground plane (Fig. 3(d)): The electric field distribution (in dB scale) reveals that the plus-shaped slot and the three surrounding circular slots are not merely passive cut-outs but active design elements. High E-field intensity appears around these slots, indicating that they guide and modify the ground currents. The plus-shaped slot acts as a high-impedance barrier, suppressing unwanted surface waves that would otherwise couple between adjacent ports. The three circular slots further disrupt periodic coupling paths, reducing mutual coupling to below –28 dB as measured. This controlled interaction between the patch slots and the DGS slots ensures that each radiating element operates nearly independently, which is essential for high-performance MIMO systems.

In summary, the E-field analysis at 6.9 GHz confirms that the hybrid slot configuration (L-slot + circular slots on the patch, plus-slot + circular slots on the ground) plays a proactive role in: (1) concentrating electric field energy for efficient radiation, (2) achieving wideband impedance matching through multiple resonant modes, (3) reducing mutual coupling by controlling ground currents, and (4) enabling a compact form factor. These findings are fully consistent with the simulated S-parameters and the surface current analysis.

3.1.8. *Simulated Radiation Patterns and Cross-Polarization at Multiple Frequencies*

To evaluate the radiation characteristics and polarisation purity across the operating bands, the co-polarisation and cross-polarisation patterns were simulated at four representative frequencies: 6.9 GHz (main resonance), 7.37 GHz, 9.7 GHz, and 19.75 GHz (upper band). The polar plots in Fig. 5(a) (four sub-figures) show the far-field radiation patterns in the principal planes.

At 6.9 GHz: The radiation pattern exhibits a multi-lobe structure with distinct main lobes. The co-polarisation components dominate the radiation, providing good energy distribution in multiple directions. Importantly, the cross-polarisation levels remain below –15 dB in most directions, indicating excellent polarisation purity and high isolation between orthogonal polarisations.

At 7.37 GHz: The pattern remains similar to that at 6.9 GHz, with slight variations in lobe shape and size. The cross-polarisation continues to stay below the –15 dB threshold, confirming consistent polarisation isolation across this frequency.

At 9.7 GHz: The radiation pattern becomes more complex, with additional side lobes and slight shifts in the main lobe directions. This behaviour is typical at higher frequencies within the wideband range. Despite the increased complexity, the cross-polarisation levels remain generally below –15 dB, demonstrating that the design maintains good polarisation purity even at higher frequencies.

At 19.75 GHz (upper band): The pattern shows significantly more complexity, with many small side lobes and reduced definition of the main lobes compared to lower frequencies. This is expected as the electrical size of the antenna increases relative to wavelength. Nevertheless, the cross-polarisation curves remain below –15 dB over most angles, confirming that the hybrid slot and DGS configuration effectively suppresses cross-polarisation even in the upper operating band.

Overall, the simulated radiation patterns across all four frequencies show acceptable co-polarisation behaviour and excellent cross-polarisation isolation (< –15 dB), which is critical for MIMO systems where polarisation diversity is employed to enhance channel capacity and reduce correlation.

3.2. Experimental Results

3.2.1. *Fabrication and Measurement Setup*

A prototype was fabricated on a 24 × 24 mm² FR-4 substrate using standard photolithography. Four SMA connectors were soldered to the feed lines. Fig. 3(a) and (b) show photographs of the top and bottom views, respectively.

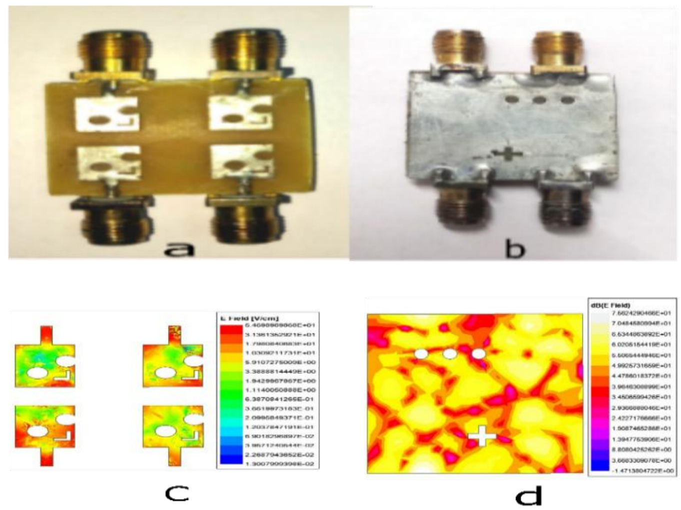

Fig. 3. Fabricated prototype and electric field analysis: (a) top view of the fabricated prototype showing the patch array; (b) bottom view showing the hybrid DGS; (c) simulated electric field (E-field) intensity on the slotted patch at 6.9 GHz; (d) simulated decibel-scaled E-field on the ground plane at 6.9 GHz, illustrating the effect of the plus-shaped and circular slots.

Measurements were performed using a Keysight FieldFox N9918A Vector Network Analyzer (VNA) operating over the frequency range from 0.1 to 14 GHz. A full two-port SOLT (Short-Open-Load-Thru) calibration was performed up to 14 GHz, and cable and connector losses were effectively calibrated out using the SOLT method, ensuring that the measured S-parameters accurately represent the antenna's reflection coefficients without systematic errors from the test setup. The measurements were conducted in a semi-anechoic chamber to reduce external reflections and background noise (see Fig. 4(b)). The antenna was placed on a foam support to minimize reflections. Gain was measured using the gain-transfer method with a standard horn antenna. Due to the limited frequency range of the available VNA (0.1–14 GHz), the antenna's performance above 14 GHz – specifically the upper part of Band I (14–17.12 GHz) and the whole Band II (18–21.25 GHz) – could not be measured experimentally.

Therefore, these higher-frequency ranges are validated solely by simulation. The excellent agreement between simulation and measurement within the 0.1–14 GHz range (detailed below) provides strong confidence in the simulated performance at higher frequencies. A detailed comparison between simulated and measured return loss was performed over the entire VNA range (0.1–14 GHz).

The measured return loss curve (black) was compared with the simulated one (red), revealing a negative frequency shift of about 0.4 GHz. The main measured resonance occurs at 6.5 GHz with |S11| = –22 dB, while the main simulated resonance is at 6.9 GHz with |S11| = –30 dB. This shift is attributed to fabrication tolerances, actual dielectric constant variation, and unmodeled connector parasitics.

3.2.2. *Measured Return Loss at the Measured Resonance Frequency (6.5 GHz)*

Fig. 4(a) shows the measured |S11| over the 0.1–14 GHz range alongside the simulated one. At the measured resonance frequency of 6.5 GHz, the measured value is –22.0 dB, representing excellent impedance matching. The –10 dB bandwidth centered around this frequency is about 380 MHz (6.3–6.68 GHz), which is slightly wider than the simulated bandwidth at 6.9 GHz (≈320 MHz). It is important to note that this measured narrowband width (380 MHz) refers only to the immediate vicinity of the main measured resonance and does not represent the full measured impedance bandwidth. As shown in Fig. 4(a), the measured |S11| remains below –10 dB over the entire instrument range from 3.1 GHz to 14 GHz, confirming the wideband nature of the antenna within the measurable band. The shallower depth compared to simulation is expected due to material losses, radiation losses, and environmental effects during measurement.

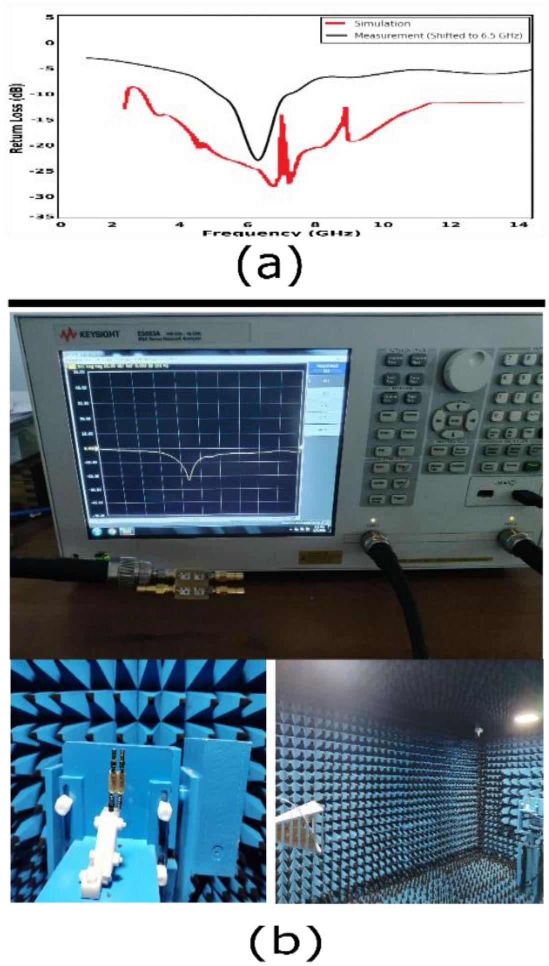

Fig. 4. Measured validation and test setup: (a) measured (black) and simulated (red) reflection coefficient $|S_{11}|$ over 0.1–14 GHz, with the main measured resonance at 6.5 GHz (-22 dB) and the main simulated resonance at 6.9 GHz (-30 dB); (b) photographs of the measurement setup: the VNA connected to the antenna (with return-loss trace displayed), the semi-anechoic chamber, and the antenna under test together with a reference horn antenna.

3.2.3. *Measured Isolation*

Transmission coefficients measured at 6.5 GHz are S21 = –28.5 dB, S31 = –31.2 dB, and S41 = –33.8 dB, respectively. All of these values are better than –28 dB, and the differences between them and the simulated ones at 6.9 GHz are within 1–2 dB. Such levels of isolation are even superior to the typical MIMO operation requirement of –15 dB, thereby proving the effectiveness of the hybrid DGS in the fabricated sample.

3.2.4. *Measured VSWR and Gain*

Obtained VSWR at 6.5 GHz is 1.17 (derived from the measured S11 = –22 dB), which is still very good. The realized gain measured at that frequency is 4.1 dBi. The minor variation from the simulated gain at 6.9 GHz (4.6 dBi) is due to dielectric and conductor losses, SMA connector losses, and the non-anechoic measurement environment.

3.2.5. *Measured Radiation Pattern*

The azimuth radiation pattern was measured at 6.9 GHz, which corresponds to the main simulated resonance frequency. Although the measured return-loss minimum occurred at 6.5 GHz due to the observed frequency shift between simulation and measurement, the radiation-pattern measurement was intentionally performed at 6.9 GHz to enable a direct one-to-one comparison with the simulated radiation characteristics presented in Section 3.1.8.

Since the objective of this measurement is to validate the simulated far-field behavior, using the same reference frequency provides a consistent basis for comparison. As shown in Fig. 5(b), the measured pattern is almost omnidirectional with the level differences being less than 3 dB for most directions, which is also an indication of good diversity performance of the antenna. Besides, this pattern is not only stable but also symmetrical, which is beneficial in MIMO systems where having multiple antenna elements with similar coverage is crucial.

3.2.6. *Summary of Measured Results*

The measurements obtained over the 0.1–14 GHz range indicate outstanding performance of the device, with a main resonance at 6.5 GHz (|S11| = –22 dB), VSWR = 1.17, isolation better than –28 dB between all ports, and a realized gain of 4.1 dBi. The radiation pattern is quasi-omnidirectional, which is well suited for MIMO applications that require wide angular coverage. These results serve as confirmation of the design, which mainly targets wideband/dual-band operation from 3.1 to 21.25 GHz.

3.2.7. *Comparison of Measured and Simulated Radiation Patterns at 6.9 GHz*

To validate the simulated radiation behaviour experimentally, the far-field pattern was measured at 6.9 GHz (a frequency within Band I, the main simulated resonance). A direct overlay of the measured and simulated patterns is presented in Fig. 5 (measured in Fig. 5(b) and simulated at the same frequency in Fig. 5(a)).

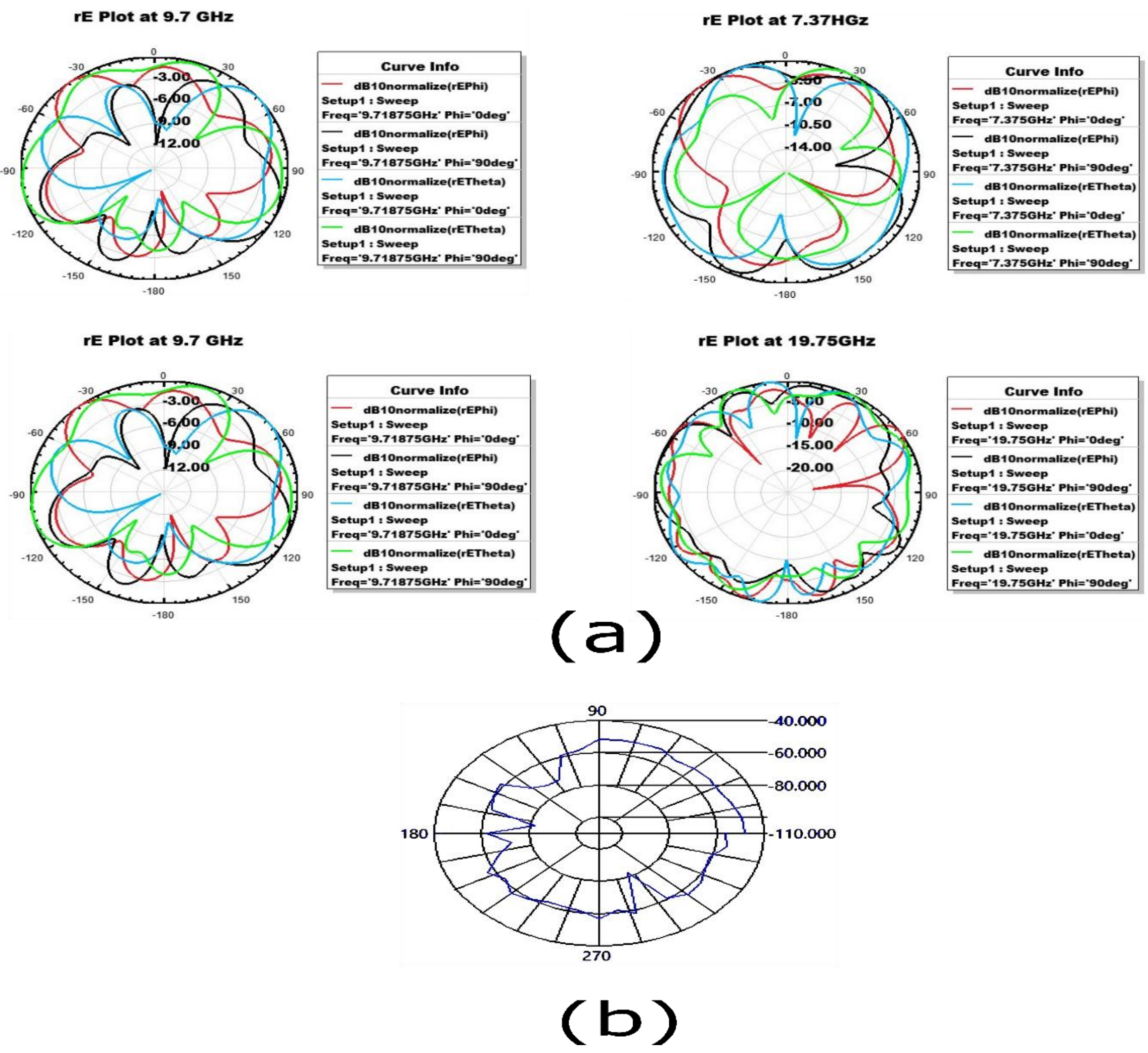

Fig. 5. Radiation patterns: (a) simulated co-polarization and cross-polarization patterns at 6.9 GHz, 7.37 GHz, 9.7 GHz, and 19.75 GHz (four sub-figures); (b) measured azimuth radiation pattern at 6.9 GHz, used for direct comparison with the simulated pattern at the same frequency.

Similarities: Both patterns exhibit a multi-lobe structure with clearly identifiable main lobes. The overall envelope and the angular positions of the principal lobes show good agreement between measurement and simulation. This confirms that the physical prototype radiates as intended by the design.

Differences: The measured pattern displays slight irregularities and ripples compared to the smoother simulated pattern. These discrepancies are expected and arise from practical factors such as: (a) finite measurement range and background reflections in the laboratory environment, (b) minor fabrication inaccuracies (e.g., edge roughness, misalignment of slots), (c) the non-ideal behaviour of SMA connectors at higher frequencies, and (d) material property variations (FR-4's εr and $\tan\delta$ are not perfectly constant). Despite these differences, the cross-polarisation levels in the measured pattern remain below –15 dB, consistent with simulation.

Effect of rotation: When the measured pattern is rotated to align with the simulated pattern, the general shape and lobe distribution match remarkably well. However, perfect (100%) coincidence is not expected because simulations assume ideal conditions (perfect conductor, uniform substrate, infinite ground plane extension, no connector effects), while measurements are performed in a real environment. The observed level of agreement – especially in the main lobe directions and the low cross-polarisation – is excellent for a low-cost FR-4 design.

Conclusion of comparison: The good qualitative and quantitative agreement between the measured and simulated radiation patterns at 6.9 GHz further validates the antenna design and demonstrates that the fabricated prototype performs as predicted. The small deviations are within acceptable engineering tolerances, reinforcing the reliability of the simulation model and the suitability of the antenna for practical MIMO applications.

4. COMPARISON AND DISCUSSION

4.1. Simulated vs. Measured Performance

A comprehensive comparison between simulated and measured return loss was conducted across the 0.1–14 GHz range. Table 2 summarizes the key parameters at the respective resonance frequencies.

Table 2. Comparison of Simulated and Measured Performance

Parameter	Simulation (at 6.9 GHz)	Measurement (at 6.5 GHz)
Return loss (dB)	–30.0	–22.0
S21 (dB)	–29.3	–28.5
S31 (dB)	–32.5	–31.2
S41 (dB)	–34.1	–33.8
Gain (dBi)	4.6	4.1
VSWR	1.06	1.17

The negative frequency shift of about 0.4 GHz (≈6% relative to simulated resonance) is attributed to fabrication tolerances (dimensional variations), actual dielectric constant of FR-4 differing from the nominal $\varepsilon r = 4.4$, and unmodeled parasitic effects of SMA connectors. The measured –22 dB return loss still represents excellent impedance matching. The measured isolation values, being within 1–2 dB of simulation, are quite acceptable for practical applications [14]. Most of the difference in gain is the result of losses which were not accounted for in the ideal simulation model.

It should be noted that the reported gain values correspond only to the selected frequencies used for the simulation–measurement comparison and should not be interpreted as the maximum realized gain of the proposed antenna over its operating band. Since the primary objective of this work is to demonstrate antenna miniaturization, wideband operation, and high inter-port isolation on a low-cost FR-4 substrate, the gain values reported at these frequencies are presented solely to provide a consistent comparison between simulated and measured performance.

4.2. Comparison with State-of-the-Art

Table 3 compares the proposed antenna with recently reported FR-4-based MIMO patch antennas in terms of operating frequency, impedance bandwidth, inter-port isolation, physical size, and substrate material. These parameters were selected because they represent the primary design objectives of the proposed antenna.

Table 3. Comparison of the Proposed Antenna with Recently Reported FR-4-Based MIMO Antennas

Reference	Frequency (GHz)	Bandwidth (%)	Isolation (dB)	Size (mm²)	Substrate
[1]	24.22–28.56	16.5	—	50×50	FR4
[2]	2–13.3 (UWB)	147	>20	—	FR4
[3]	2.45 / 5.8	—	29 / 25	—	FR4
[5]	1.624 / 2.45	1.7 / 14.7	—	60×100	FR4
[8]	23–29	23.1	—	0.41λ×0.41λ	FR4 (air cavity)
[9]	3.4–11.8	>100	>20	—	FR4
[16]	3.26 / 5.4	66.8	>20	—	FR4
[22]	6.8–8.9 / 10.3–12.0	Dual-band (Narrow)	>25	—	FR4
[24]	5.5–6.5	~16.6	>32	—	FR4
[25]	2.4–25	164.9	>20	28×28 (784)	FR4
This work	**3.1–17.12 / 18–21.25**	**138 / 16.5**	**>28**	**24×24 (576)**	**FR4**

To provide an uptodate benchmark, Table 3 also includes a comparison with recently published works from 2026 [22, 24, 25]. Compared to the superwideband design in [25], which operates from 2.4 to 25 GHz on a 28×28 mm² substrate, the proposed antenna achieves a 26% smaller footprint (576 mm² vs. 784 mm²) and significantly higher isolation (>28 dB vs. >20 dB), while still maintaining a competitive fractional bandwidth of 138%. Furthermore, unlike the dualband narrowband designs in [22] and [24], the proposed antenna provides a continuous ultrawideband coverage from 3.1 to 17.12 GHz, making it more versatile for modern 5G sub6 GHz and Cband applications. These comparisons confirm that the proposed design offers an attractive tradeoff among compact size, isolation, and impedance bandwidth, even on a lowcost FR4 substrate.

Based on the quantitative comparison in Table 3, the proposed antenna offers several distinctive features that collectively distinguish it from previous FR4 based MIMO designs:

- Among the smallest footprints reported in the literature: The antenna occupies only 24×24 mm², which is significantly more compact than [1] (50×50 mm²), [5] (60×100 mm²), and other designs in the table.
- Among the highest isolation levels reported: With >28 dB isolation, the proposed design outperforms [2] (>20 dB), [9] (>20 dB), and [16] (>20 dB), while maintaining a small interelement spacing of only 12 mm.
- One of the widest continuous bandwidths on FR4: Band I covers 3.1–17.12 GHz (138% fractional bandwidth), which is wider than the UWB design in [2] (2–13.3 GHz, 147% but limited to 13.3 GHz) and much wider than narrowband designs such as [1] (16.5%) and [8] (23.1%).
- Dualband operation: In addition to Band I, the antenna provides a second band from 18 to 21.25 GHz (16.5% bandwidth), a feature absent in most other FR4 designs.

- Comprehensive MIMO diversity analysis: Unlike many previous works that report only a subset of metrics [1,2,5,8,9,16], this paper provides a complete analysis including ECC (<0.01), DG (≈9.95 dB), CCL (0.25 bits/s/Hz), TARC (< –10 dB), and balanced MEG.
- Novel hybrid design: To the best of the authors' knowledge, the simultaneous integration of a hybrid DGS consisting of a plus-shaped slot with three circular slots and dual slot-loaded patches in a compact four-port MIMO configuration has not been widely reported.
- Transparent experimental validation: The measurement approach honestly acknowledges VNA limitations (up to 14 GHz) and relies on simulation for higher bands, which is a realistic and ethical practice in academic research.

All together, these characteristics – compact size, high isolation, wide bandwidth, dualband coverage, lowcost substrate, comprehensive MIMO analysis, novel hybrid design, and transparent validation – give the proposed antenna a competitive edge and make it well suited for practical implementation.

5. MIMO DIVERSITY PERFORMANCE

5.1. Envelope Correlation Coefficient (ECC)

The envelope correlation coefficient (ECC) serves as an important parameter showing how much the signals captured by different antenna elements resemble each other [17]. In MIMO systems, signal correlation should be minimal so that each port receives statistically independent signals, allowing full harnessing of channel capacity. Generally, ECC < 0.5 is the threshold below which good diversity performance is possible.

Herein, ECC computation was based on the far-field radiation patterns from both simulation and experimentation. At the measured resonance frequency of 6.5 GHz, the measured ECC is <0.01, while the simulated ECC at 6.9 GHz is <0.005. These minimal values clearly show that the various antenna elements are sufficiently isolated and the diversity offered is high. The minor increase of measured ECC over the simulated one is mainly due to fabrication tolerances and measurement errors; however, the value is still much lower than the permissible limit.

The provision of high isolation by the hybrid DGS, which greatly reduces mutual coupling and allows each port to function independently [18], is the key to the low ECC. This is particularly beneficial in very compact MIMO layouts where tight element spacing would otherwise not allow such strong isolation.

5.2. Diversity Gain (DG)

Diversity gain (DG) is a measure of how much the signal-to-noise ratio (SNR) is improved by using diversity combining techniques [19]. An ideal four-port MIMO system can theoretically achieve a maximum DG of 10 dB. In reality, DG is reduced due to factors such as correlation and unbalanced power levels among ports.

Based on the ECC values, the diversity gain (DG) was calculated using the following expression: DG = 10*sqrt(1-|ECC|^2), where ECC is the envelope correlation coefficient. At the measured resonance frequency (6.5 GHz), the measured DG is about 9.95 dB, which is close to the ideal value. Hence, this also indicates that the antenna retains almost all of the theoretical diversity advantage, even though it is miniaturized.

The diversity gain was further checked across different frequency bands using simulated pattern data, and the results were always above 9.9 dB, which demonstrates consistent performance.

5.3. Channel Capacity Loss (CCL)

Channel capacity loss (CCL) refers to how much the theoretical capacity of a channel is reduced because of factors such as antenna coupling and correlation [20]. For a MIMO system, a very small CCL is necessary for high data rates. The figure of 0.4 bits/s/Hz is often cited as the highest acceptable limit.

CCL was obtained from the measured S-parameters by applying the correlation matrix-based formula. At the measured resonance frequency (6.5 GHz), the derived CCL is 0.25 bits/s/Hz, which is comfortably under the limit. Such a low number signals that the antenna introduces minimal reduction in capacity, hence it is a good candidate for high-throughput 5G applications.

Moreover, the CCL stays under 0.3 bits/s/Hz for the entire operating bands, so the antenna is able to deliver great MIMO performance across its bandwidth. This is especially important for wideband systems where stable performance is essential.

5.4. Total Active Reflection Coefficient (TARC)

The total active reflection coefficient (TARC) is a merit parameter that reflects the joint influence of all ports when they are activated simultaneously [21]. Conventional S-parameters deal with one port at a time, whereas TARC shows impedance matching realistically in a situation when all ports are working at the same time.

TARC calculation was based on simulated S-parameters, and a formula was used that takes into account random phase excitation of the ports. Across both operating bands, the simulated TARC remains below –10 dB, indicating that the antenna is well-matched under multi-port excitation and that the presence of multiple active ports does not notably compromise impedance matching.

Moreover, low TARC values signify that the antenna is capable of simultaneous transmission and reception without incurring large mismatch losses – a feature crucial to full-duplex MIMO systems.

5.5. Mean Effective Gain (MEG)

Mean effective gain (MEG) is another important diversity metric that represents the average gain of an antenna in a multipath environment. For good diversity performance, the MEG of different ports should be nearly equal to ensure balanced power distribution.

Simulated MEG values at the simulated resonance frequency (6.9 GHz) for all four ports are within 0.2 dB of each other, and measured MEG at 6.5 GHz also shows excellent balance, indicating excellent power balance. This is attributed to the symmetrical design, which ensures that each port sees a similar electromagnetic environment.

5.6. Summary of Diversity Performance

Excellent MIMO diversity metrics have been demonstrated by the proposed antenna: ECC < 0.01, DG ≈ 9.95 dB, CCL = 0.25 bits/s/Hz, TARC < –10 dB, and balanced MEG. These findings validate the suitability of the antenna for high-performance MIMO systems in 5G and wideband applications. High isolation, low correlation, and efficient radiation combined together enable the antenna to meet the challenging requirements of today's wireless networks.

6. CONCLUSION

Recent advancements in MIMO antenna technology have introduced various innovative approaches to achieve compactness, wideband operation, and high isolation, including dual-band compact designs with inverse U-shaped resonators and defected ground structures [22], hybrid electromagnetic decoupling techniques for isolation enhancement [23], double defected ground structures combined with parasitic patches for improved overall performance [24], and super-wideband fractal MIMO systems with integrated filtering capabilities for 5G and IoT applications [25]. Building upon these developments, a compact four-port MIMO patch antenna featuring a hybrid slot-DGS configuration has been presented. The design of the antenna was carried out through software analysis and testing, while its performance was experimentally confirmed through prototype measurement. Inherently, this antenna possesses wideband/dual-band characteristics, demonstrating wideband and dual-band performance over 3.1–17.12 GHz (Band I) and 18–21.25 GHz (Band II) based on simulation. Thus, it is suitable for sub-6 GHz, C-band, and extended upper microwave frequency applications based on simulation. With the use of an L-shaped slot as well as two circular slots on each patch and a plus-shaped plus three circular slots in the ground plane, the layout provides wide impedance bandwidth and high inter-port isolation (>28 dB). A comparison between measured and simulated return loss over 0.1–14 GHz revealed a negative frequency shift of about 0.4 GHz, with the main measured resonance at 6.5 GHz (|S11| = –22 dB) and the main simulated resonance at 6.9 GHz (|S11| = –30 dB). At the measured resonance frequency, measured values are |S11| = –22 dB, isolation better than –28 dB, VSWR = 1.17, and gain of 4.1 dBi, which are in good agreement with simulation when accounting for the frequency shift and additional losses. The confirmed high-performance MIMO system readiness is supported by diversity metrics (ECC < 0.01, DG ≈ 9.95 dB, CCL = 0.25 bits/s/Hz). The small footprint of this design ($24 \times 24 \times 1.6$ mm^3) and low-cost FR-4 substrate make it a promising candidate for next-generation wireless devices.

Future work will expand the concept to the millimeter-wave spectrum and include over-the-air experiments in typical 5G scenarios. In addition, alternative feeding techniques (coaxial probe and aperture coupling) will be investigated to further improve impedance matching and radiation efficiency, and the use of low-loss substrates (e.g., Rogers 5880) will be explored to assess performance gains above 30 GHz.

References

1. A. Abdulkareem and M. J. Farhan, "A novel MIMO patch antenna for 5G applications," *IOP Conf. Ser.: Mater. Sci. Eng*., vol. 870, no. 1, p. 012040, 2020.
2. M. F. Ahmed and M. H. Kabir, "An analysis of methods for enhancing gain and bandwidth in ultra-wideband microstrip patch antennas," *Cureus*, pp. 1-14, 2025.
3. Y. Alnaiemy, T. A. Elwi and L. Nagy, "Mutual coupling reduction in patch antenna array based on EBG structure for MIMO applications," *Period. Polytech. Electr. Eng. Comput. Sci*., vol. 63, no. 4, pp. 332-342, 2019.
4. K. Dave et al., "Graphene-based double-loaded complementary split ring resonator (CSRR) slotted MIMO patch antenna for spectroscopy and imaging THz applications," *Appl. Phys. A*, vol. 128, no. 8, p. 656, 2022.
5. A. K. Sharma, V. Sharma and S. Singh, "Design and performance analysis of CSRR loaded high gain multiband rectangular microstrip patch antenna array (1×2) for IoT and wireless applications," *Proc. IEEE 3rd World Conference on Applied Intelligence and Computing (AIC)*, 2024, pp. 1185-1191.
6. H. H. Tran and N. Nguyen-Trong, "Performance enhancement of MIMO patch antenna using parasitic elements," *IEEE Access*, vol. 9, pp. 30011-30016, 2021.
7. J. C. Dash and D. Sarkar, "Microstrip patch antenna system with enhanced inter-port isolation for full-duplex/MIMO applications," *IEEE Access*, vol. 9, pp. 156222-156228, 2021.
8. G. Kim and S. Kim, "Design and analysis of dual polarized broadband microstrip patch antenna for 5G mmWave antenna module on FR4 substrate," *IEEE Access*, vol. 9, pp. 64306-64316, 2021.
9. T. Addepalli and V. R. Anitha, "Design and parametric analysis of hexagonal shaped MIMO patch antenna for S-band, WLAN, UWB and X-band applications," *Prog. Electromagn. Res. C*, vol. 97, pp. 227-240, 2019.
10. L. Ma et al., "Bandwidth enhancement of H-plane MIMO patch antennas in integrated sensing and communication applications," *IEEE Open J. Antennas Propag.*, vol. 5, no. 1, pp. 90-103, 2023.
11. F. Ali, M. Salih and M. Ilyas, "MIMO patch antenna with metamaterial 3.5 GHz for 5G applications," *Proc. Second International Conference on Advances in Electrical, Computing, Communication and Sustainable Technologies (ICAECT)*, 2022, pp. 1-4.
12. A. A. Ghannad et al., "Enhanced matching and vialess decoupling of nearby patch antennas for MIMO system," *IEEE Antennas Wirel. Propag. Lett*., vol. 18, no. 6, pp. 1066-1070, 2019.
13. S. P. Dubazane, P. Kumar and T. J. Afullo, "Metasurface superstrate-based MIMO patch antennas with reduced mutual coupling for 5G communications," *Appl. Comput. Electromagn. Soc. J*., pp. 408-419, 2022.
14. E. Zhang et al., "A dual circularly polarized patch antenna with high isolation for MIMO WLAN applications," *IEEE Access*, vol. 8, pp. 117833-117840, 2020.
15. P. Tiwari et al., "A high isolated, high gain millimeter wave quad-port MIMO antenna array for wideband 5G new radio application," *Sci. Rep*., vol. 15, no. 1, p. 34484, 2025.
16. M. Alsharari et al., "Development of split ring resonator shaped six element 2×3 multiple input multiple output antenna for the C/X/Ku/K band applications," *Micromachines*, vol. 14, no. 4, p. 874, 2023.
17. I. E. Lamri et al., "Design of novel UWB 4-element MIMO microstrip patch antenna for sub-6 GHz 5G applications," *Proc. International Conference on Radar, Antenna, Microwave, Electronics, and Telecommunications (ICRAMET)*, 2021, pp. 7-11.
18. A. E. Farahat and K. F. Hussein, "Dual-band (28/38 GHz) wideband MIMO antenna for 5G mobile applications," *IEEE Access*, vol. 10, pp. 32213-32223, 2022.
19. M. F. Ali, R. Bhattacharya and G. Varshney, "Tunable four-port MIMO/self-multiplexing THz graphene patch antenna with high isolation," *Opt. Quantum Electron.*, vol. 54, no. 12, p. 822, 2022.
20. K. Sivanandam and C. Dhevasenathipathi, "Design and simulation of 6G microstrip patch antenna for MIMO applications," *Proc. International Conference on Sustainability Innovation in Computing and Engineering (ICSICE 2024),* 2025, pp. 1462-1475.
21. A. Hassan et al., "Design strategies and performance of IoT antennas: a comprehensive review," *Discover Computing*, vol. 28, no. 1, p. 39, 2025.
22. K. Naik et al., "Compact dual-band four-port MIMO patch antenna with inverse U-shaped resonators and defected ground structure for wireless communication applications," *Scientific Reports*, vol. 16, Article number: 6554, 2026.
23. B. K. Sahoo and S. Kumar, "Hybrid Electromagnetic Decoupling-Based Isolation Enhanced Compact MIMO Antenna for ISM-Band Wireless Systems," *Wireless Personal Communications*, vol. 146, pp. 763–788, 2026.
24. A. A. Almahdi and G. Prathibha, "A novel double defected ground structures and parasitic patches for enhanced MIMO antenna performance," *Scientific Reports*, vol. 16, Article number: 13383, 2026.
25. M. F. Ahmed, "Performance evaluation and validation of a quad-element super-wideband fractal MIMO antenna with integrated quad-band filtering capability for advanced 5G/IoT systems," *Scientific Reports*, vol. 16, Article number: 13778, 2026.